Atomic-layer-deposited amorphous MoS_2 for durable and flexible Li-O_2 batteries

Ming Song, Hua Tan, Xianglin Li, Alfred Iing Yoong Tok, Pei Liang, Dongliang Chao, Hong Jin Fan**

Dr. M. Song
College of Chemistry and Chemical Engineering
Xuzhou University of Technology
Xuzhou 221111, China

Dr. M. Song, H. Tan, Dr. D. Chao, Prof. H. J. Fan*
School of Physical and Mathematical Sciences
Nanyang Technological University
Singapore 637371, Singapore
Email: S120055@e.ntu.edu.sg
Email: fanhj@ntu.edu.sg

H. Tan
State Key Laboratory of Crystal Material
Shandong University
Jinan 250100, China

Dr. X. Li, Prof. A. I. Y. Tok
School of Material Science and Engineering
Nanyang Technological University
Singapore 639798, Singapore

Prof. P. Liang
College of Optical and Electronic Technology
China Jiliang University
Hangzhou 310038, China

Keywords: Li-O_2 battery; MoS_2; integrated cathode; atomic layer deposition; flexible battery

Abstract

Li-O_2 batteries (LOB) potentially have the highest specific capacity among all types of metal-ion batteries but suffer severally from cycle instability and low energy efficiency. In this work, we fabricate an integrated cathode that contains amorphous MoS_2 thin layer deposited on 3D conductive carbon scaffold to improve the energy efficiency to ~83% and cycle life up to 190 cycles. We employ an advanced pressure-tuned stop-flow atomic layer deposition (ALD) method to deposit an ~5 nm thick amorphous MoS_2 layer on carbon nanotubes (CNT) forests covered graphite foam. It is established that this integrated 3D cathode exhibits high catalytic activity for both oxygen reduction reaction (ORR) and oxygen evolution reaction (OER). The benefit of the ALD MoS_2 in lowering the energy barrier is also supported by first-principles calculations. Finally, we also assemble quasi-solid state flexible LOBs that can be stably discharged up to 6 days. This new and rational design of cathode may provide a new direction for achieving high-performance flexible Li-O_2 batteries.

Main Text

There have been continuous interests and commercial demands in developing new batteries with higher gravimetric energy densities than the current Li-ion batteries. Li-O_2 batteries (LOBs) have the highest theoretical specific energy among all batteries, which is 3500 Wh Kg^{-1} based on the ideal electrochemical reaction $2Li + O_2 \leftrightarrow Li_2O_2$.[1] Li-$O_2$ batteries are regarded as the “Holy Grail” of batteries and have attracted immense interest since 1996.[2-15] However, LOBs have their “Achilles’ Heel”: parasitic reactions severely limit their cycle life, energy efficiency and specific capacity.[16] In general, the vexing parasitic chemistry mainly involves degradation of cathode materials and electrolyte components,[17] in which reduced oxygen species (O_2^-, O_2^{2-}, etc.) and singlet oxygen ($^1O_2$ or $^1\Delta_g$) play a pivotal role.[18] Thus, there is a consensus that the key player of LOBs is a stable cathode material with high activity for oxygen reduction reaction (ORR) and oxygen evolution reaction (OER).

Among all kinds of cathode materials in LOBs, the carbon material, especially carbon nanotubes (CNT) and graphene, is most popular because of its merits of high conductivity, low cost, good ORR activity, large specific surface, and tunable nanostructure.[19-20] However, the drawback of pure carbon materials is the inevitable corrosion during the discharge/charge process.[21-22] Therefore, surface protection is needed for stability enhancement of carbon materials. In addition, for bi-functionality of the LOB cathode, it is also necessary to combine carbon with other OER electrocatalysts, as carbon is mainly ORR active. In this regard, the highly conductive and flexible carbon nanomaterials become effective support to the OER catalysts with a possible synergistic effect between them, which has been well reviewed recently.[23]

In LOBs, various transition metal based electrocatalysts have been studied, as summarized in a few recent Reviews.[24-25] Transition metal dichalcogenides (TMDs),

such as MoS_2, have become the protagonist in different areas including optoelectronics, biosensors, catalysis, energy storage and conversion.[26] MoS_2 is intrinsically a stable and promising electrocatalyst for hydrogen evolution reaction (HER) in acidic solution,[27] but its ORR/OER activity is rather limited. While there are a few reports on utilization of MoS_2 in LOBs (for example, MoS_2 nanosheets/Au nanoparticles through hydrothermal synthesis,[28] MoS_2 nanoflakes by liquid exfoliation method[29-30]), the battery performances, especially cycle life and rate capability, are relatively poor due to the low activity and limited $O_2/Li^+/e^-$ transmission capability.

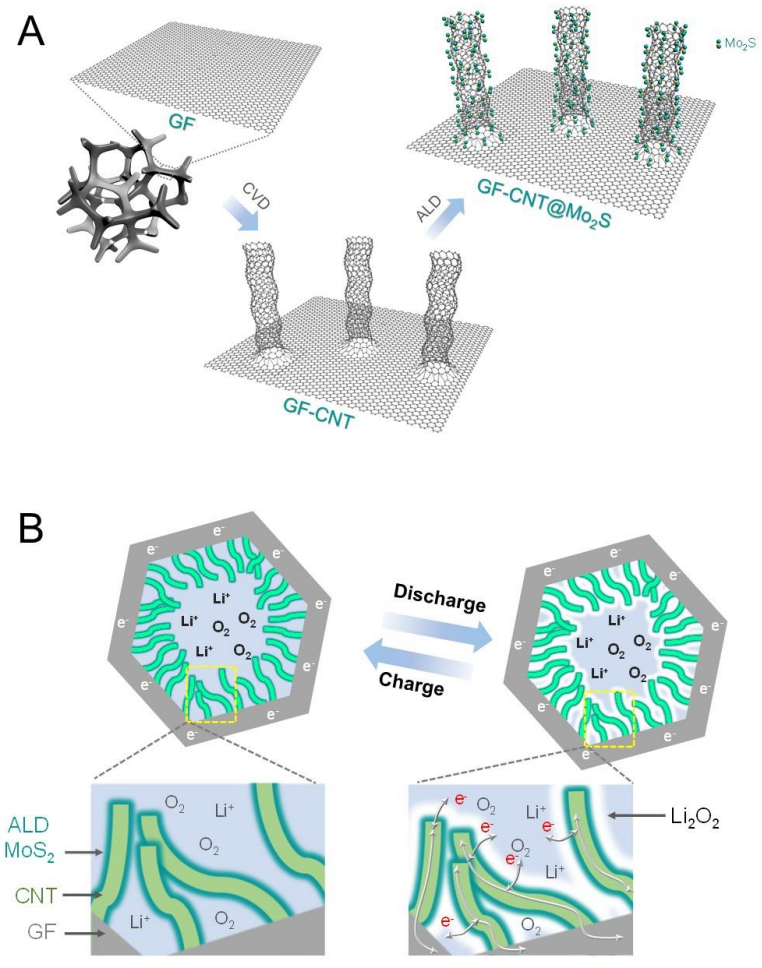

Figure 1. Schematics of A) the fabrication and B) charge and discharge process of the GF-CNT@MoS_2 integrated cathode in Li-O_2 battery.

Recently, it is found that MoS_2 nanoparticles with disordered structure can improve the OER and ORR activities.[31-32] Atomic layer deposition is an effective method for uniform deposition of low-amount OER/ORR catalyst materials on conductive matrix.[33] Inspired by this and above, herein, we design and realize a new integrated cathode, denoted as GF-CNT@MoS_2, where amorphous MoS_2 is deposited on carbon nanotubes (CNT) substrates growing on a 3D graphite foam (GF) current collector, through a pressure-tuned stop-flow atomic layer deposition (ALD) process. The synthesis process of this GF-CNT@MoS_2 cathode is illustrated in **Figure 1A**. First, a flexible and light-weight 3D GF (**Figure S1)** was employed as the current collector and substrate for the growth of CNT network by a standard chemical vapor deposition method. The purpose is to construct a hierarchical carbon structure with higher specific surface for loading MoS_2, continuous conductivity network, and good flexibility. Then, a pressure-tuned stop-flow ALD method, which is a powerful technique for the deposition of uniform thin film on 3D nanostructures,[34],[35] was implemented to deposit amorphous MoS_2 using $Mo(CO)_6$ and $C_2H_6S_2$ as precursors (details of synthesis process are in the Experimental Section). With this judicious design of new cathode, we achieved a LOB cell that exhibits significantly enhanced performance in terms of energy efficiency and cycle stability.

The rationality of this design lies in the following two aspects (also see Figure 1B):

1) Improved OER/ORR activity and stability from the synergistic effect of amorphous MoS_2 and CNT (denoted as CNT@MoS_2). First, the CNT network has intrinsic ORR activity, and the MoS_2 coating thickness is not uniform on the entire surface, based on our TEM observations. So the ions can still either penetrate the thin amorphous MoS_2 or directly reach the uncovered CNT surface. Second, the CNT network will mainly provide sufficient deposition surfaces and electrical conductivity to promote the

OER/ORR activity of amorphous MoS_2. In the meantime, the amorphous MoS_2 can protect CNT against parasitic reaction with electrolyte so that a stable cathode can be achieved.

2) High $O_2/Li^+/e^-$ transmission ability from the hierarchical structure of CNT and 3D GF. The interconnected macro-pores of 3D GF framework ensure easy access of oxygen and electrolyte (Li^+) to the inner space of the cathode. CNT functions as the high-speed electron transmitter between MoS_2 and GF.

The amorphous structure of the just deposited MoS_2 thin film is verified by X-ray diffraction (XRD) and Raman investigations (see details in **Figure S2**, Supplementary Information). Transmission electron microscopy (TEM) and scanning electron microscopy (SEM) observations were carried out to reveal the morphologic difference between the samples with and without the deposited MoS_2. As shown in **Figure 2A**, one of the representative CNTs with a tubular structure is obviously observed. These CNTs with diameters of around 20 nm intertwine and construct a continuous conductivity network (Figure 2C). This CNT network also provides sufficient surface and interspace for ALD MoS_2. After ALD, the overall morphology of the CNT network retains except for increases in thickness (Figure 2B). The thickness of uniform MoS_2 layer is about 5 nm and there are still sufficient gaps between the CNT@MoS_2 (Figure 2D), which provides space for the accommodation of discharge products (i.e. Li_2O_2). It has been proposed that 5-10 nm is the critical thickness of Li_2O_2, above which the charge transport from cathodes to the Li_2O_2/electrolyte interface will not be sufficient to support the electrochemical reaction of LOBs.[37] Thus, in order to ensure good transport kinetics, we optimize the ALD cycles (50 cycles in this case) so that the remaining gaps among CNT@MoS_2 is in the range of 10-20 nm (Figure 2D). The MoS_2 content in the as-synthesized GF-CNT@MoS_2 is determined to be about 29.3 wt %

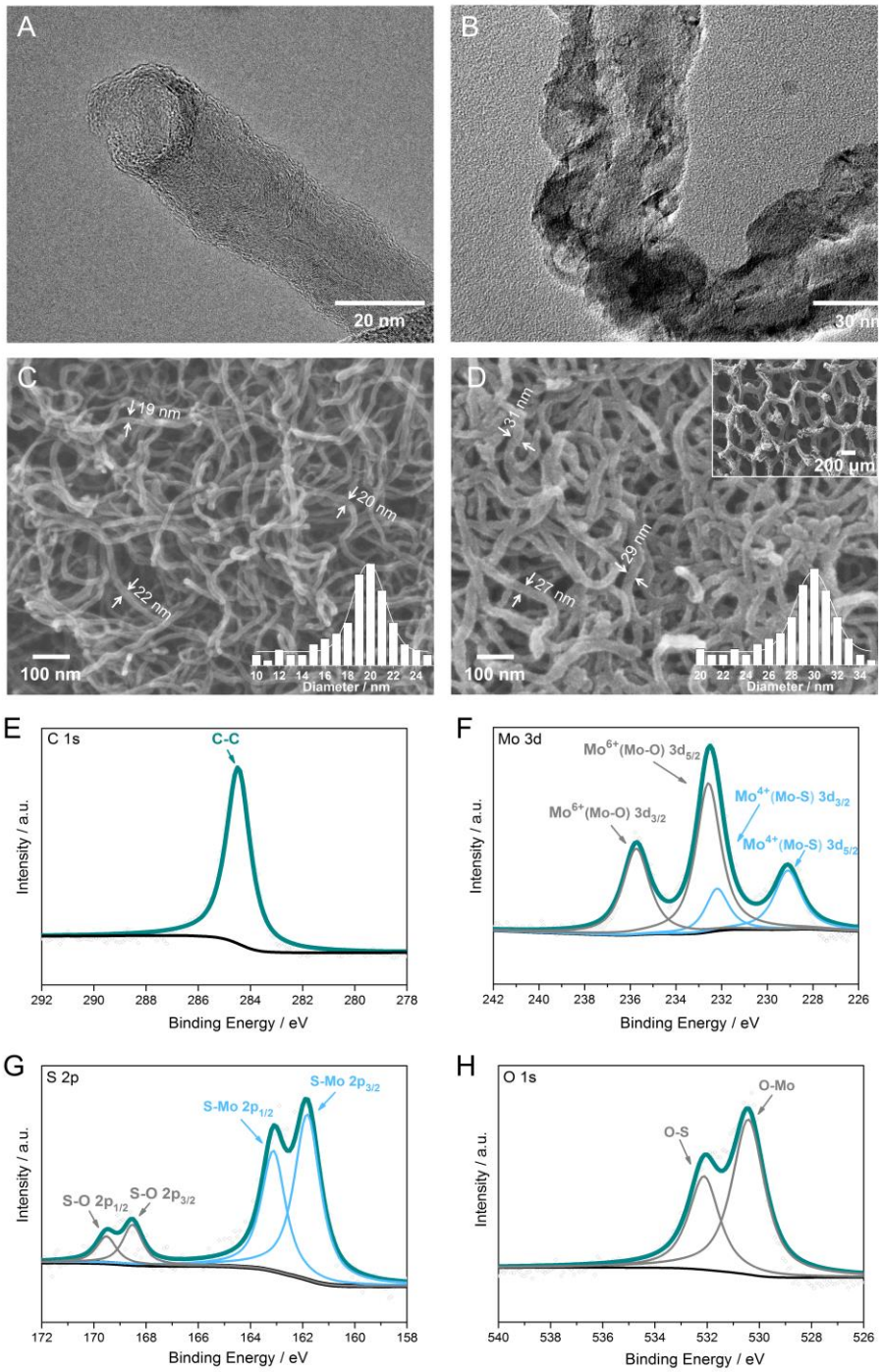

Figure 2. Characterization of the as-fabricated GF-CNT@MoS_2. TEM images of (A) CNT and (B) CNT@MoS_2 after ALD amorphous MoS_2. (C) SEM image of CNTs uniform grown on graphite foam (GF-CNT). (D) SEM image of GF-CNT@MoS_2. Insets in C and D are the histograms of the diameter distribution before and after ALD, respectively. A clear increase in the diameter can be seen. The corresponding EDX elemental mapping of the GF-CNT@MoS_2 is presented in Figure S2 (supplementary information). (A-D) XPS spectra of the as-fabricated GF-CNT@MoS_2, showing the C 1s, Mo 3d, S 2p, and O 1s spectra. In addition to MoS_2, MoO_3 phase is also identified due to partial surface oxidation.

(Figure S2C). Energy dispersive X-ray (EDX) elemental mapping further reveals the Mo and S elements on CNT (Figure S2D). In addition, the weak signal of O element is also found which may come from the partial oxidation on the surface of amorphous MoS_2 due to its high activity. Such an oxygenated surface MoS_2 is suggested beneficial for the OER activity and stability of cathodes during discharging/charging under O_2 environment.[31]

X-ray photoelectron spectroscopy (XPS) is employed to further clarify the surface composition of the as-prepared GF-CNT@MoS_2. The peak at 284.7 eV in C 1s spectra corresponds to C-C bonds of the GF@CNT (**Figure 2E**).[38-39] Binding energies at 229.1 eV (232.2 eV) and 161.8 eV (163.1 eV) are associated with Mo^{4+} $3d_{5/2}$ ($3d_{3/2}$) and S^{2-} $2p_{3/2}$ ($2p_{1/2}$) core levels in MoS_2, respectively. The peaks at 232.8 and 235.9 eV in (B) indicates the presence of Mo^{6+} (MoO_3) on the surface of MoS_2. The two low-intensity S-O peaks in the S 2p spectrum also indicate partial surface oxidation of MoS_2. Mo 3d peaks at 232.2 and 229.1 eV are identified for the doublet of Mo^{4+} $3d_{3/2}$ and Mo^{4+} $3d_{5/2}$ from MoS_2, respectively (Figure 2F).[40-41] The doublet of S^{2-} $2p_{1/2}$ and S^{2-} $2p_{3/2}$ from MoS_2 are also observed in Figure 2G (163.1 and 161.9 eV, respectively).[40-41] In addition, the spin-orbit doublet peaked at 232.8 and 235.9 eV belong to Mo^{6+} from MoO_3 (Figure 2F) due to partial oxidation.[40, 42] Meanwhile, the S element of MoS_2 is also partially oxidized according to the S 2p spectra (Figure 2G).[43-44] The partial oxidation of Mo element and S element on the outer surface of GF-CNT@MoS_2 is further verified by O 1s spectra (Figure 2H).[45-46] These XPS results are consistent with that of EDX elemental mapping (Figure S2D).

In short, it is proved by TEM, SEM, EDX, XRD, Raman, and XPS results that we have achieved a new type of GF-CNT@MoS_2 cathode with a 3D hierarchical structure. This electrode is expected to render high-performance Li-O_2 battery with flexibility and

enhanced rater performance.

To demonstrate the application of this GF-CNT@MoS_2 sample in LOBs, we characterized the electrochemical performance using home-made Swagelok-type cells using a Li metal anode, a free-standing GF-CNT@MoS_2 cathode without additional current collectors, and a glass fiber separator impregnated with electrolyte (details are in the Experimental Section).[47] The electrochemical activity of GF-CNT@MoS_2 is firstly revealed by galvanostatic discharge/charge method. **Figure 3A** shows the discharge/charge profiles of GF-CNT@MoS_2 electrodes at different current densities with a cut-off capacity of 500 mAh g^{-1}. At the current density of 250 mA g^{-1}, the average charge voltage is only 3.33 V and the overpotential gap is just 0.58 V. This indicates a remarkable OER/ORR property of the cathode and high energy efficiency (~83%). The full discharge/charge behavior of the GF-CNT@MoS_2 electrode are shown in **Figure S3**. Calculated specific capacities at different current densities are higher than those of most previously reported cathodes based on MoS_2 or CNT (**Figure S4**). For the cycling performance, the GF-CNT@MoS_2 cathodes are tested at a current density of 500 mA g^{-1} with a fixed specific capacity of 500 mAh g^{-1} (a commonly used parameter in LOBs[48-49]). As shown in Figure 3B and 4C, an outstanding performance up to 190 cycles is observed and the change of terminal voltage is smooth. Compared to previous studies, this cycling performance is also extraordinary (see detailed comparison in **Table S1**).

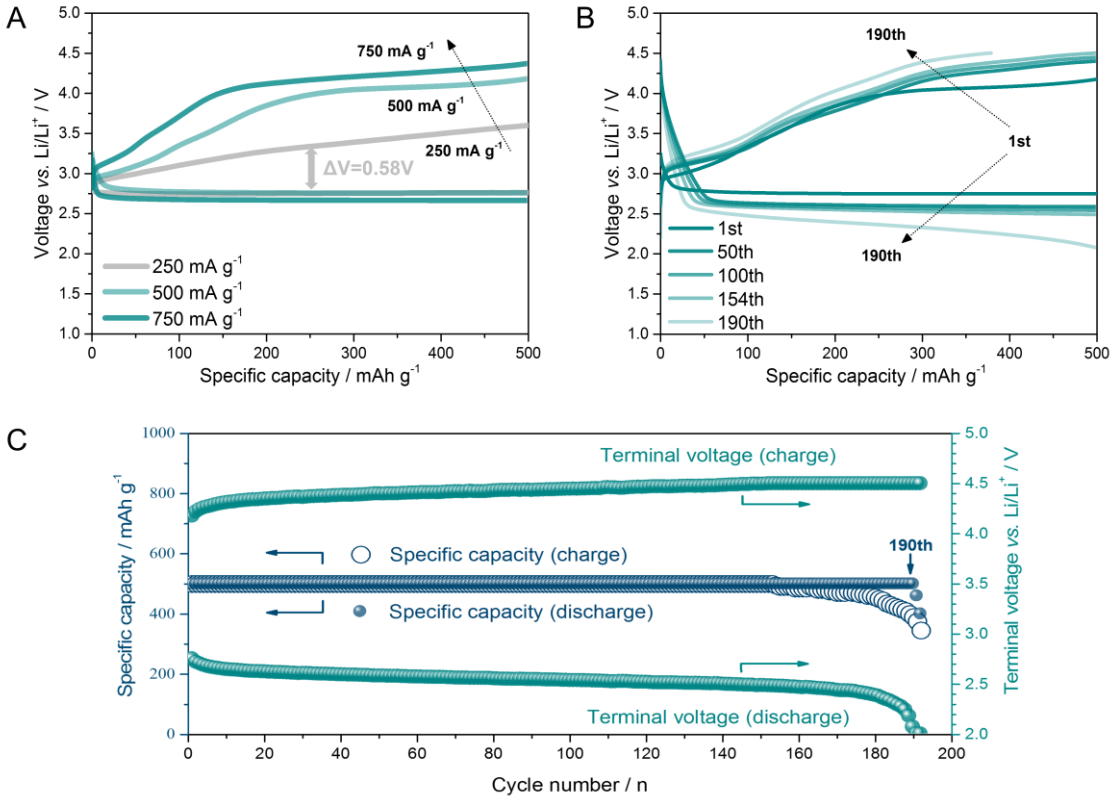

Figure 3. Li-O_2 battery performance. (A) Galvanostatic discharge/charge profiles of the cell at different current densities. The specific capacity is limited to 500 mAh g^{-1}. (B) Galvanostatic discharge/charge profiles at different cycles. The current density is 500 mA g^{-1} (0.5 mA cm^{-2}) and the specific capacity limit is 500 mAh g^{-1} (0.5 mAh cm^{-2}). (C) The cycling stability of specific capacity and terminal voltages.

In contrast, the electrochemical properties of the GF-CNT electrodes without amorphous MoS_2 are much poorer. Although the GF-CNT electrodes exhibit good ORR activity, they have lower specific capacities and higher charging overpotentials than the GF-CNT@MoS_2 electrodes (**Figure S5A**). Moreover, the GF-CNT cathode shows a poor cycling property and the terminal discharge (charge) voltages decrease (increase) to the cut-off voltages 2.0 V (4.5 V) after only 14 cycles (**Figure S6**). This cycling performance is similar to those of pure CNT cathodes reported by other researchers.[19, 48, 50] Cyclic voltammetry (CV) is further applied to understand the electrochemical behavior of GF-CNT@MoS_2 electrodes. As shown in Figure S5B, GF-

CNT@MoS_2 electrodes exhibit much lower oxidation peak potentials and higher current responses than those of GF-CNT electrodes. As to the reduction process, a higher current response and a lower polarization are obtained for GF-CNT@MoS_2. These results are consistent with the galvanostatic discharge/charge results (Figure S5A), and imply superior OER/ORR kinetics of the integrated electrode rendered by the amorphous MoS_2.

The superior electrochemical properties of the GF-CNT@MoS_2 cathode could be ascribed to the rational design. *First*, it has been proved that amorphization can effectively improve catalytic properties of materials, and the amorphous MoS_2 with a disordered structure provides abundant active edge sites and enhanced intrinsic catalytic activity.[51] *Second*, the oxygenated surface of MoS_2 has subtly modulated local coordination environments and electronic structures, which further promotes the OER catalytic activity.[31] In addition, the CNTs are quite important in our opinion: they have a good intrinsic ORR activity, but also provides sufficient surfaces for the loading of MoS_2, and as well as continuous conductivity network. All these significantly contribute to the high OER/ORR activity of the GF-CNT@MoS_2 cathodes. Meanwhile, a much longer cycle life is realized mainly because the carbon skeleton is protected by the thin ALD MoS_2 against parasitic reactions associated with singlet oxygen ($^1\Delta_g$) and reduced oxygen species (O_2^-, O_2^{2-}, etc.).[18] Hence, the synergistic effect of amorphous MoS_2 and CNT leads to the enhancement of OER/ORR activity and stability. *Last*, the light-weight and highly conductive graphite foam with interconnected 3D macro-pores should also be beneficial as it ensures an easy access of oxygen and electrolyte (Li^+) to the inner reaction interfaces of the cathode, which facilitates the O_2/Li^+/e^- transport kinetics.

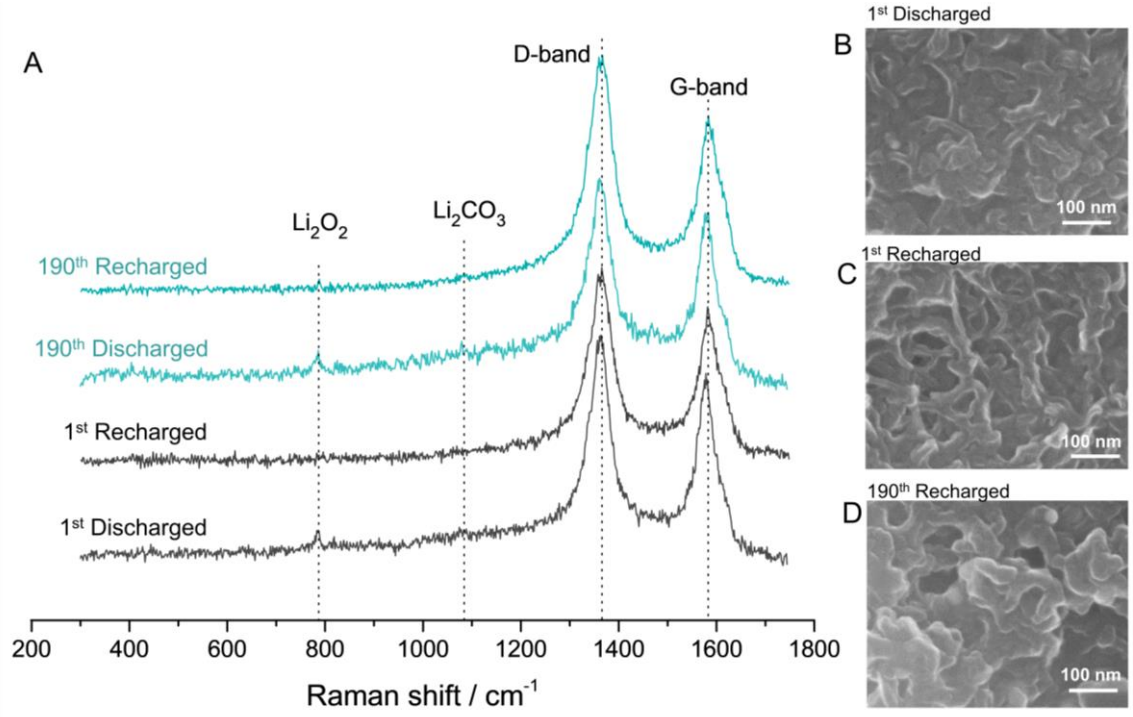

Figure 4. Post-mortem examination of the GF-CNT@MoS_2 electrode. (A) Raman spectra at different discharge/charge states. The Li_2O_2 Raman peak appears in the discharge state but disappear after recharge, but the Li_2CO_3 Raman peak is very weak in all stages. (B-D) Corresponding SEM images of the electrode surface showing the morphology change of Li_2O_2.

We further carried out Raman, SEM and EIS measurements to understand the origin of improved electrochemical performance of the GF-CNT@MoS_2 electrodes. After discharging in the first cycle, the Li_2O_2 Raman peak at 788 cm^{-1} is observed and no obvious discharge byproducts such as Li_2CO_3 (~1088 cm^{-1}) can be found, which indicates the Li/O_2 electrochemical reaction is mainly responsible for the capacity of cathodes (**Figure 4A**). As shown in the SEM image (Figure 4B), the Li_2O_2 grows uniformly on the surface of CNT@MoS_2 filling the pores. After recharging in the first cycle, the Li_2O_2 peak vanishes in the Raman spectrum and the pores also reappear (Figure 4C). Hence, the thin Li_2O_2 film can still support the charge transport from

cathodes to the Li_2O_2/electrolyte interface and it is also decomposable to a certain degree. This should account for the observed high reversibility of the GF-CNT@MoS_2 cathode. On the other hand, the Li_2O_2 cannot decompose completely after cycling for 190 times, as residues on the surface of the cathode (Figure 4D) is observed accompanied with a week Li_2O_2 Raman peak (Figure 4A). This is consistent with the result of galvanostatic discharge/charge in Figure 3. However, for the GF-CNT electrode (see Figure S6), the Li_2CO_3 peak at ~1088 cm^{-1} does not disappear after recharging. This implies an irreversible reaction and may account for, partially, the poor electrochemical performance of the GF-CNT electrode in the absence of MoS_2 (Figure S6). Furthermore, after 14 cycles, the charge-transfer resistance of GF-CNT electrode increases obviously and becomes much larger than that of GF-CNT@MoS_2 electrode (see Figure S7), which further proves the poor cycle stability of GF-CNT electrode. The increased charge-transfer resistance is related with the accumulation of the Li_2CO_3 byproduct.

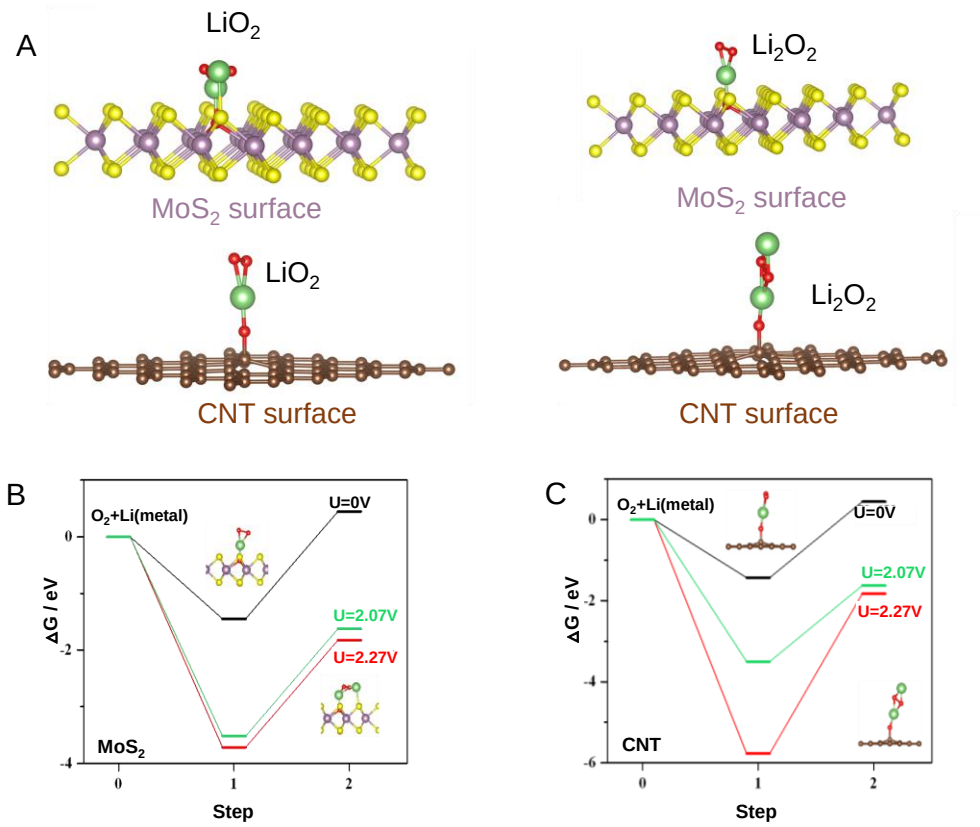

Figure 5. DFT calculation. (A) The atomic configuration of LiO_2 and Li_2O_2 absorbed on MoS_2 surface or CNT surface. Schematic free energy diagrams of oxygen reduction on (B) MoS_2 and (C) CNT surface. The reaction steps include the formation of LiO_2 (step 1) and the transformation of LiO_2 to Li_2O_2 (step 2).

In order to understand better the reaction kinetics in an atomic scale, first-principles density function theory (DFT) was carried out (see details in the Experimental Section). In a Li-O_2 battery, it is generally considered that the formation of Li_2O_2 undergoes the following two steps:

$$\text{Step 1}: \quad X\,(\text{surface}) + O_2 + Li^+ + e^- \rightarrow X - LiO_2 \qquad (1)$$

$$\text{Step 2}: \quad X - LiO_2 + Li^+ + e^- \rightarrow X - Li_2O_2 \qquad (2)$$

$$\text{or} \quad 2LiO_2 \rightarrow Li_2O_2 + O_2 \qquad (3)$$

Here, in order to simplify the calculation, only one Li_2O_2 dimer is considered (**Figure 5A**). The optimized structures of LiO_2 and Li_2O_2 on MoS_2 surface and on CNT surface

are presented in Figure 5A. The calculated values of free energy change (ΔG) under different potentials (U) for the two surfaces are shown in Figure 5B. At the reversible potential (U=2.07 V), ΔG_1 (step 1) for both MoS_2 and CNT surfaces are below 0 eV, which implies that LiO_2 is the stable intermediate on the surface. The growth mechanism of Li_2O_2 is the "solvation-mediated" pathway, which includes the diffusion of LiO_2 in electrolyte and disproportionation from LiO_2 to Li_2O_2. This is consistent with the results in Figure 4B and Figure S3. More importantly, ΔG_2 (step 2) of the MoS_2 surface is much smaller than that of CNT surface, which signifies a better kinetics capability of the amorphous MoS_2 surface.

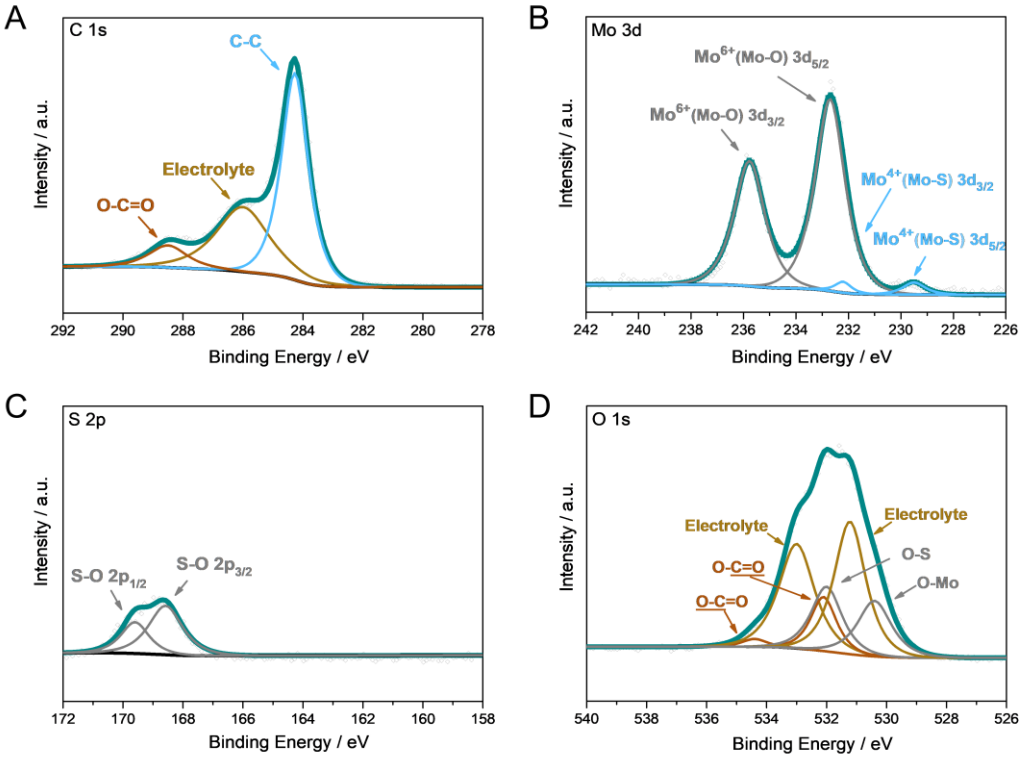

Figure 6. XPS spectra of the GF-CNT@MoS_2 cathode after cycling (190 cycles). (A) C 1s, (B) Mo 3d, (C) S 2p and (D) O 1s spectra. Comparison to the XPS result before cycling test in Figure 3 reveals surface oxidation of MoS_2.

The surface chemical state of the GF-CNT@MoS_2 electrodes after 190 cycles was examined using XPS (**Figure 6**). We need to compare the XPS result of the as-prepared sample (Figure 2) to see the change of surface chemistry. It is noticed that the peaks associated with Mo^{6+} (Mo-O) become stronger while those of Mo^{4+} (Mo-S) and S 2p spectrum due to Mo-S are both weaker. This is clear evidence of surface oxidation which is inevitable during the handling of samples. The peak at ~286.2 eV in C 1s spectrum is consistent with absorbed electrolyte (O-CH_3) (Figure 6A).[21] The weak peaks at ~288.6 eV (Figure 6A), ~534.4 eV and ~532.1 eV (Figure 6D) correspond to the O-C=O bonds which may be associated with the degradation of electrolyte or dimethyl carbonate residues (used for rinsing electrodes to remove TEGDME before XPS characterization).[52-54] Moreover, O_2 crossover that cannot be effectively blocked in organic liquid electrolytes and volume change of Li metal during cycling may also give rise to the degradation of Li anode. Hence, we propose that, the surface oxidation, combined with possible degradation of electrolyte and anode, is the reason for the final breakdown of the LOB.[30] Therefore, to further improve the cycle life of LOB, it is essential to develop stable electrolyte and construct high-efficiency Li anode.[55-56]

To further demonstrate its potential application in flexible electronics, a flexible Li-air battery (LAB) is assembled using this GF-CNT@MoS_2 cathode (**Figure 7A**). As shown in Figure 7B-E, a commercial temperature and relative humidity indicator are powered by this flexible LAB under various bent and twisted conditions. Moreover, the flexible LABs can last more than 6 days when they are rolled or crumpled (Figure 7F). As mentioned above, the inherent mechanical flexibility of the 3D GF current collector and the integrated GF-CNT@MoS_2 electrode provide this remarkable flexibility and mechanical robustness. Furthermore, the flexible LAB can also survive when it is

partially immersed in water aided by a waterproof oxygen-permeable film (Figure 7B).

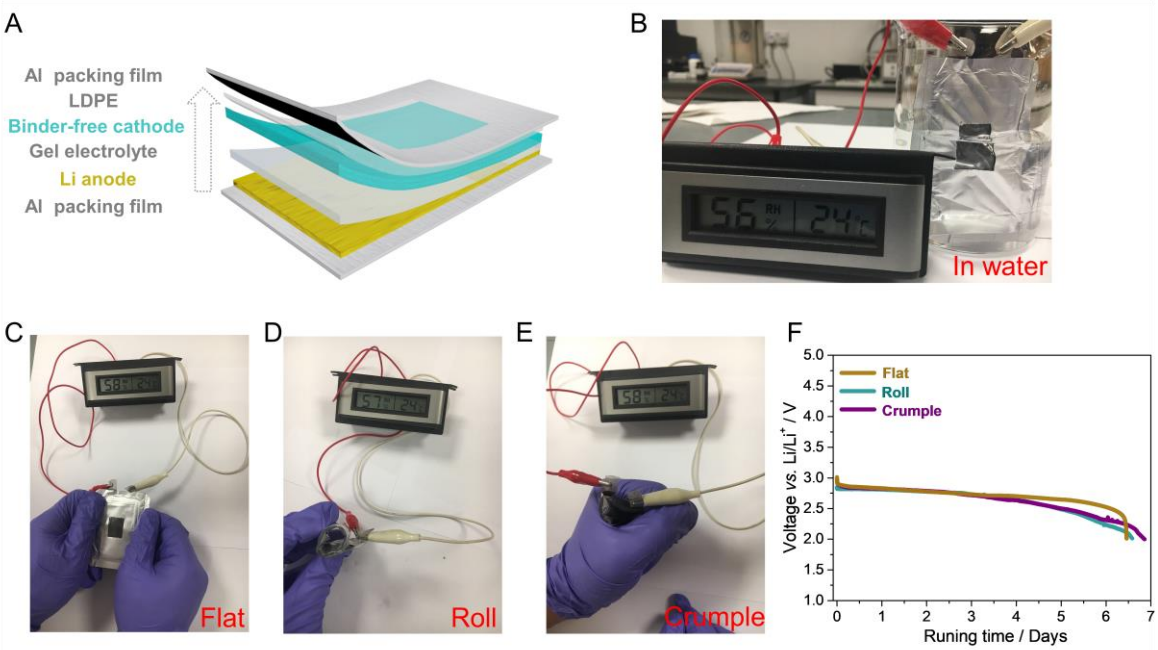

Figure 7. Demonstration of a flexible Li-O_2 full battery. (A) Schematic of the flexible LOB using the GF-CNT@MoS_2 cathode and quasi-solid gel electrolyte. Photographs of the LOB that powers a commercial temperature and relative humidity indicator when the battery is (B) immersed in water, (D-E) flatted, rolled or crumpled. (F) Continuous discharge profiles at the constant current of 0.05 mA cm^{-2} of the LOB under different condition. The equivalent capacity is about 7200 mAh g^{-1}.

In summary, we have presented a smart GF-CNT@MoS_2 integrated cathode with amorphous ALD MoS_2 deposited on the hierarchical structure of GF@CNT. This rational design renders multiple benefits and has thus significantly enhanced the LOB performance. The LOBs exhibit a high energy efficiency of 83% at 250 mA g^{-1}, a long cycle life of 190 cycles and a high capacity of 4844 mAh g^{-1} at 500 mA g^{-1}. DFT calculation proves that the amorphous MoS_2 layer with a disordered structure provides abundant catalytic active sites and better kinetics, which is responsible for the high OER/ORR activity and long cycle life. In the meantime, the thin MoS_2 layer protects the CNTs and maintains their intrinsic ORR activity of the CNTs by preventing direct

parasitic reactions. The highly conductive, lightweight, and macroporous GF-CNTs network has facilitated ions/gas transport, maintained the high activity during long cycles, and offered mechanical flexibility of the LOB cell. Our results provide a new way of designing high-performance cathodes to boost the cycling stability of LOBs.

Experimental Section

Synthesis of GF@CNT@MoS_2.

A piece of hydrophilicity-treated 3D graphite foam (GF) current collector (~0.5 mg cm^{-2}, prepared by the CVD method according to our previous work[39, 57]) was used to grow carbon nanotubes (CNT). GF was immersed into an ethanol/ethylene glycol mixed solution (volume ratio is 95:5) containing 0.22 M $Ni(NO_3)_2$ for 30 min. After drying at 90 °C for 30 mins, it was put into quartz tube furnace under the mixed gas flow of Ar (140 sccm)/H_2 (10 sccm) and heated to 600 °C in 20 mins. Then, ethanol was bubbled into the quartz tube by the mixed gas flow at 600 °C for 5 mins. After this CVD reaction, GF@CNT was formed and taken out to be cooled down rapidly and the mass loadings of CNT was 0.6 mg cm^{-2}. MoS_2 was further deposited on GF@CNT through a pressure tuned stop-flow atomic layer deposition (ALD) method according to our previous work.[34] Briefly speaking, the precursors $Mo(CO)_6$ were first pulsed in the reactor, then N_2 was filled in to increase the base pressure of the reactor (6 mbar was used here). The dimethyl disulfide (DMDS) precursor was introduced with the same process after twice pluses of $Mo(CO)_6$. These precursors were kept in the reactor for 5 s, then excess precursors and byproducts were purged out prior to the next half cycle. The precursor delivery lines were maintained at 80 °C and the reaction chamber was held at 150 °C. After 50 cycles, GF@CNT@MoS_2 was obtained and the mass loadings of MoS_2 was 0.4 mg cm^{-2}.

Characterization.

XRD patterns were performed on a Bruker-AXS D8 Advance X-ray diffractometer (CuKα, λ=1.54186). Raman spectra were collected with a laser wavelength of 532 nm using WITec-CRM200 Raman system. The morphology was observed by a field emission scanning electron microscopy (FESEM, JEOL 7600F) and a high-resolution transmission electron microscope (HRTEM, JEOL 2100F). The XPS measurements were performed by a VG ESCALAB 220i-XL system using a monochromatic Al Kα1 source (1,486.6 eV). Thermogravimetric analysis (TGA) was carried out under air flow with a heating rate of 10 °C min^{-1} on a PerkinElmer STA6000.

LOB assembly and electrochemical measurements.

Swagelok-type cells were fabricated for the electrochemical measurements. We assembled home-made Swagelok-type cells in a glovebox filled with pure argon gas (<0.5 ppm H_2O and O_2), using a Li metal anode, a free-standing GF-CNT@MoS_2 cathode without conventional current collectors, and a Whatman glass fiber separator impregnated with an electrolyte containing 1 M LiTFSI (bis(trifluoromethane)sulfonimide lithium salt) in TEGDME (tetraethylene glycol dimethyl ether). The galvanostatic discharge/charge experiments were

conducted with a Neware battery tester at different current densities at the room temperature. The discharge capacities were calculated based on the weight of CNT and MoS_2 (1.0 mg cm^{-2}) on GF current collector. Cyclic voltammetry (CV) and electrochemical impedance spectroscopy (EIS) experiments were conducted on a CHI 660E electrochemical workstation. The voltage range of CV was 2.3-4.3 V and the sweep rate was 0.03 mV s^{-1}. EIS were obtained in the frequency range from 1 MHz to 100 MHz with an AC amplitude of 5 mV.

For the flexible LOB cell, the anode was obtained by rolling Li pellet on stainless steel mesh. The precursor solution of the gel electrolyte was synthesized by dissolving 1g poly(vinylidene fluoride-co-hexafluoropropylene) (PVDF-HFP) in 4g N-methyl-2-pyrrolidinone (NMP), which was then mixed with 3g ethoxylated trimethylolpropanetriacrylate (ETPTA), 0.01g 2-hydroxy-2-methyl-1-phenyl-1-propanone (HMPP) and 2ml 1 M LiTFSI in TEGDME. The precursor solution was cast on the anode followed by 365 nm UV irradiation for about 20 s to produce a solid gel electrolyte. Lastly, the anode covered with the gel electrolyte was assembled with the GF@CNT@MoS_2 cathode in a punched aluminum plastic film with a waterproof oxygen-permeable film (low-density polyethylene, LDPE).

DTF calculation.

All the calculations were performed using first-principles density function theory (DFT) with the VASP package. The projected-augmented wave (PAW) method was applied to treat the ion-electron interactions. The exchange-correlation energy of electrons was calculated in the generalized gradient approximation (GGA) scheme with the PBE functional parameterization. The energy cut-off was 400 eV, and the energy criterion of the self-consistent convergence was placed as at 0.00001 eV $atom^{-1}$. For body phase calculation, the k-point sampling in the first Brillouin zone is 10×10×10. Here the free energy difference (ΔG) is only considered as the total energy difference (ΔE), which could be got through DFT calculation. The MoS_2 mono-layer is constructed with six layers and 4×4 two-dimensional supercell, an O atom is instead a S atom to form the defective MoS_2 (the defect concentration is 3.125%), and the LiO_2 and Li_2O_2 cluster absorbed on the supercell, and the vacuum layer is more than 20.0 Å. Herein, graphene layer was used in our model to model the CNT considering the large diameter of CNT and the heavy load, and in order to avoid the interaction between the LiO_2 and Li_2O_2, the 5×5 two-dimensional supercell was used. And the LiO_2 and Li_2O_2 cluster absorbed on the graphene layer supercell, and the vacuum layer is more than 20.0 Å. The k point sampling in the first Brillouin zone is set as 8×8×1.

Acknowledgements

M. Song and H. Tan contribute equally to this work. M. Song is thankful to funds from the Science Foundation of Jiangsu Province (BK20171169). Financial support by the China Scholarship Council (No. 201708320127 and No. 201706220185) to academic visits to the Nanyang Technological University, Singapore is appreciated. H. J. Fan acknowledges the support by Singapore Ministry of Education AcRF Tier 1 grant (RG10/18) and Tier 2 grant (MOE2017-T2-1-073).

References

[1] X. Gao, Y. Chen, L. R. Johnson, Z. P. Jovanov, P. G. Bruce, *Nat. Energy* **2017**, *2*, 17118.

[2] L. Luo, B. Liu, S. Song, W. Xu, J.-G. Zhang, C. Wang, *Nat. Nanotechnol.* **2017**, *12*, 535.

[3] J. Lu, Y. J. Lee, X. Luo, K. C. Lau, M. Asadi, H.-H. Wang, S. Brombosz, J. Wen, D. Zhai, Z. Chen, *Nature* **2016**, *529*, 377.

[4] H.-D. Lim, B. Lee, Y. Zheng, J. Hong, J. Kim, H. Gwon, Y. Ko, M. Lee, K. Cho, K. Kang, *Nat. Energy* **2016**, *1*, 16066.

[5] X. Gao, Y. Chen, L. Johnson, P. G. Bruce, *Nat. Mater.* **2016**, *15*, 882.

[6] D. Aurbach, B. D. McCloskey, L. F. Nazar, P. G. Bruce, *Nat. Energy* **2016**, *1*, 16128.

[7] T. Liu, M. Leskes, W. Yu, A. J. Moore, L. Zhou, P. M. Bayley, G. Kim, C. P. Grey, *Science* **2015**, *350*, 530.

[8] N. B. Aetukuri, B. D. McCloskey, J. M. García, L. E. Krupp, V. Viswanathan, A. C. Luntz, *Nat. Chem.* **2015**, *7*, 50.

[9] L. Johnson, C. Li, Z. Liu, Y. Chen, S. A. Freunberger, P. C. Ashok, B. B. Praveen, K. Dholakia, J.-M. Tarascon, P. G. Bruce, *Nat. Chem.* **2014**, *6*, 1091.

[10] M. M. O. Thotiyl, S. A. Freunberger, Z. Peng, Y. Chen, Z. Liu, P. G. Bruce, *Nat. Mater.* **2013**, *12*, 1050.

[11] Y. Chen, S. A. Freunberger, Z. Peng, O. Fontaine, P. G. Bruce, *Nat. Chem.* **2013**, *5*, 489.

[12] Z. Peng, S. A. Freunberger, Y. Chen, P. G. Bruce, *Science* **2012**, 1223985.

[13] S. H. Oh, R. Black, E. Pomerantseva, J.-H. Lee, L. F. Nazar, *Nat. Chem.* **2012**, *4*, 1004.

[14] H.-G. Jung, J. Hassoun, J.-B. Park, Y.-K. Sun, B. Scrosati, *Nat. Chem.* **2012**, *4*, 579.

[15] K. Abraham, Z. Jiang, *J. Electrochem. Soc.* **1996**, *143*, 1.

[16] A. C. Luntz, B. D. McCloskey, *Chem. Rev.* **2014**, *114*, 11721.

[17] A. C. Luntz, B. D. McCloskey, *Nat. Energy* **2017**, *2*, 17056.

[18] N. Mahne, B. Schafzahl, C. Leypold, M. Leypold, S. Grumm, A. Leitgeb, G. A. Strohmeier, M. Wilkening, O. Fontaine, D. Kramer, *Nat. Energy* **2017**, *2*, 17036.

[19] X.-Y. Yang, J.-J. Xu, Z.-W. Chang, D. Bao, Y.-B. Yin, T. Liu, J.-M. Yan, D.-P. Liu, Y. Zhang, X.-B. Zhang, *Adv. Energy Mater.* **2018**, *8*, 1702242.

[20] G. Tan, L. Chong, R. Amine, J. Lu, C. Liu, Y. Yuan, J. Wen, K. He, X. Bi, Y. Guo, H. H. Wang, R. Shahbazian-Yassar, S. Al Hallaj, D. J. Miller, D. Liu, K. Amine, *Nano Lett.* **2017**, *17*, 2959.

[21] B. D. McCloskey, A. Speidel, R. Scheffler, D. Miller, V. Viswanathan, J. Hummelshøj, J. Nørskov, A. Luntz, *The journal of physical chemistry letters* **2012**, *3*, 997.

[22] M. M. Ottakam Thotiyl, S. A. Freunberger, Z. Peng, P. G. Bruce, *J. Am. Chem. Soc.* **2013**, *135*, 494.

[23] Y.-J. Wang, B. Fang, D. Zhang, A. Li, D. P. Wilkinson, A. Ignaszak, L. Zhang, J. Zhang, *Electrochemical Energy Reviews* **2018**, *1*, 1.

[24] Z. Chang, J. Xu, X. Zhang, *Adv. Energy Mater.* **2017**, *7*, 1700875.

[25] S. Yang, P. He, H. Zhou, *Energy Storage Mater.* **2018**, *13*, 29.

[26] X. Zhang, Z. Lai, Q. Ma, H. Zhang, *Chem. Soc. Rev.* **2018**, *47*, 3301.

[27] X. Geng, W. Sun, W. Wu, B. Chen, A. Al-Hilo, M. Benamara, H. Zhu, F. Watanabe, J. Cui, T.-p. Chen, *Nat. Commun.* **2016**, *7*, 10672.

[28] P. Zhang, X. Lu, Y. Huang, J. Deng, L. Zhang, F. Ding, Z. Su, G. Wei, O. G. Schmidt, *J. Mater. Chem. A* **2015**, *3*, 14562.

[29] M. Asadi, B. Kumar, C. Liu, P. Phillips, P. Yasaei, A. Behranginia, P. Zapol, R. F. Klie, L. A. Curtiss, A. Salehi-Khojin, *ACS Nano* **2016**, *10*, 2167.

[30] M. Asadi, B. Sayahpour, P. Abbasi, A. T. Ngo, K. Karis, J. R. Jokisaari, C. Liu, B. Narayanan, M. Gerard, P. Yasaei, X. Hu, A. Mukherjee, K. C. Lau, R. S. Assary, F. Khalili-Araghi, R. F. Klie, L. A. Curtiss, A. Salehi-Khojin, *Nature* **2018**, *555*, 502.

[31] J. Hou, B. Zhang, Z. Li, S. Cao, Y. Sun, Y. Wu, Z. Gao, L. Sun, *ACS Catalysis* **2018**, *8*, 4612.

[32] T. Wang, D. Gao, J. Zhuo, Z. Zhu, P. Papakonstantinou, Y. Li, M. Li, *Chem. Eur. J.* **2013**, *19*, 11939.
[33] C. Zhao, C. Yu, M. N. Banis, Q. Sun, M. Zhang, X. Li, Y. Liu, Y. Zhao, H. Huang, S. Li, *Nano Energy* **2017**, *34*, 399.
[34] X. Li, M. Puttaswamy, Z. Wang, C. K. Tan, A. C. Grimsdale, N. P. Kherani, A. I. Y. Tok, *Appl. Surf. Sci.* **2017**, *422*, 536.
[35] M. Leskelä, M. Ritala, *Angew. Chem. Int. Ed.* **2003**, *42*, 5548.
[36] D. Chao, C. Zhu, M. Song, P. Liang, X. Zhang, N. H. Tiep, H. Zhao, J. Wang, R. Wang, H. Zhang, *Adv. Mater.* **2018**, 1803181.
[37] V. Viswanathan, K. S. Thygesen, J. Hummelshøj, J. K. Nørskov, G. Girishkumar, B. McCloskey, A. Luntz, *J. Chem. Phys.* **2011**, *135*, 214704.
[38] Y. Li, W. Zhou, H. Wang, L. Xie, Y. Liang, F. Wei, J.-C. Idrobo, S. J. Pennycook, H. Dai, *Nat. Nanotechnol.* **2012**, *7*, 394.
[39] D. Chao, X. Xia, J. Liu, Z. Fan, C. F. Ng, J. Lin, H. Zhang, Z. X. Shen, H. J. Fan, *Adv. Mater.* **2014**, *26*, 5794.
[40] S. Hussain, J. Singh, D. Vikraman, A. K. Singh, M. Z. Iqbal, M. F. Khan, P. Kumar, D.-C. Choi, W. Song, K.-S. An, *Sci. Rep.* **2016**, *6*, 30791.
[41] R. Zhang, Y. Li, J. Qi, D. Gao, *Nanoscale Res. Lett.* **2014**, *9*, 586.
[42] P. Qin, G. Fang, W. Ke, F. Cheng, Q. Zheng, J. Wan, H. Lei, X. Zhao, *J. Mater. Chem. A* **2014**, *2*, 2742.
[43] G. Li, J. Sun, W. Hou, S. Jiang, Y. Huang, J. Geng, *Nat. Commun.* **2016**, *7*, 10601.
[44] S. K. Yong, W. M. Skinner, N. S. Bolan, E. Lombi, A. Kunhikrishnan, Y. S. Ok, *Environ. Sci. Pollut. Res.* **2016**, *23*, 1050.
[45] T. Lei, Y. Xie, X. Wang, S. Miao, J. Xiong, C. Yan, *small* **2017**, *13*, 1701013.
[46] J. Song, X. Ni, D. Zhang, H. Zheng, *Solid State Sciences* **2006**, *8*, 1164.
[47] M. Song, D. Zhu, L. Zhang, X. Wang, L. Huang, Q. Shi, R. Mi, H. Liu, J. Mei, L. W. Lau, *J. Solid State Electrochem.* **2013**, *17*, 2061.
[48] Y. Zhou, Z. Lyu, L. Wang, W. Dong, W. Dai, X. Cui, Z. Hao, M. Lai, W. Chen, *J. Mater. Chem. A* **2017**, *5*, 25501.
[49] J. Huang, B. Zhang, Z. Bai, R. Guo, Z.-L. Xu, Z. Sadighi, L. Qin, T.-Y. Zhang, G. Chen, B. Huang, J.-K. Kim, *Adv. Funct. Mater.* **2016**, *26*, 8290.
[50] W.-J. Kwak, T.-G. Kang, Y.-K. Sun, Y. J. Lee, *J. Mater. Chem. A* **2016**, *4*, 7020.
[51] X. Zhang, Z. Luo, P. Yu, Y. Cai, Y. Du, D. Wu, S. Gao, C. Tan, Z. Li, M. Ren, *Nature Catalysis* **2018**, *1*, 460.
[52] R. A. Quinlan, Y.-C. Lu, D. Kwabi, Y. Shao-Horn, A. N. Mansour, *J. Electrochem. Soc.* **2016**, *163*, A300.
[53] B. Sivaranjini, R. Mangaiyarkarasi, V. Ganesh, S. Umadevi, *Sci. Rep.* **2018**, *8*, 8891.
[54] B. Jiang, C. Zhu, Y. Huang, *PloS One* **2015**, *10*, 0127735.
[55] C. Zhao, J. Liang, Q. Sun, J. Luo, Y. Liu, X. Lin, Y. Zhao, H. Yadegari, M. N. Banis, R. Li, *Small Methods* **2019**, *3*, 1800437.
[56] C. Zhao, Z. Wang, X. Tan, H. Huang, Z. Song, Y. Sun, S. Cui, Q. Wei, W. Guo, R. Li, *Small Methods* **2019**, 1800546.
[57] X. Liu, D. Chao, D. Su, S. Liu, L. Chen, C. Chi, J. Lin, Z. X. Shen, J. Zhao, L. Mai, *Nano Energy* **2017**, *37*, 108.